RSC Advances

PAPER

View Article Online
View Journal | View Issue

Cite this: *RSC Adv.*, 2025, **15**, 16792

A facile plant and chemical-mediated mechanosynthesis of α-Fe_2O_3 nanoparticles†

Tshegofatso M. Rabalao,[ab] Busiswa Ndaba,[*c] Ashira Roopnarain[bd] and Banele Vatsha[*a]

Received 3rd April 2025
Accepted 12th May 2025

DOI: 10.1039/d5ra02321a

rsc.li/rsc-advances

Mechanochemical reactions are highly favourable owing to their efficiency and require less or no solvents for extraction and synthesis, agreeing with green chemistry principles. Here, we explore the formation of iron(III) oxide nanoparticles using a chemical base and/or plant material in neat and liquid-assisted grinding (LAG). Interestingly, nanorods were formed by neat grinding, whilst LAG resulted in spherical-like nanoparticles when the chemical base was used. Using *Artemisia afra* as a base instead of chemical base, ultra small nanoparticles were produced showing spherical-like shape by neat grinding and polyhedral shape by LAG reaction. The morphological observation also revealed that changing the metal precursor to iron sulphate or iron nitrate influences the shape of nanoparticles formed to hexagonal and spherical-like, respectively. The conditions of the mechanochemical approach employed to synthesise iron oxide nanoparticles confirmed the production of a hematite (α-Fe_2O_3) polymorph. The mechanosynthesis protocol presents a green approach for producing new and/or existing materials at a shorter reaction time and ambient conditions in comparison to other conventional methods reported.

1 Introduction

An unremitting interest in developing iron oxide nanoparticles has been witnessed in the past three decades, which necessitates new, simple synthetic protocols for controlling shape and size. In particular, the wide range of magnetic properties (antiferromagnetic, weak ferromagnetic to ferromagnetic and superparamagnetic) of iron oxides led many investigations to tune specific size and shape for the intended application.[1,2] Iron(III) oxides have five major crystalline polymorphs, namely, α-Fe_2O_3, γ-Fe_2O_3, ε-Fe_2O_3, β-Fe_2O_3, and ζ-Fe_2O_3. Interestingly, they all have different magnetic and structural properties.[1,2] The common polymorphs found in nature are α-Fe_2O_3 and γ-Fe_2O_3, with the former being the most thermodynamically stable.[1,2] The other polymorphs are metastable and can be synthesised in the lab, often requiring high temperatures and extreme pressure conditions. These materials can be assembled on the nanoscale, resulting in a larger surface area in comparison to their bulk phase, which is beneficial to many applications, including catalysis,[3] solar cell,[4] environmental protection,[5] clinical diagnosis[6] and gas sensors.[7] A handful of synthetic methods have been investigated, including sol–gel,[8,9] precipitation,[10,11] hydrothermal,[12] microwave-assisted,[13] and solid-state reactions.[14] Mechano-chemistry is a new chemical innovation that has gained prominence as an alternative to solution chemistry.[15,16] It involves the chemical and physical changes of solids induced by a mechanical force. This solid-state approach has been used in organic transformations,[17,18] catalysis,[19–21] metal–organic framework synthesis,[22,23] as well as the synthesis of metal and/or metal oxide nanoparticles.[14,24] It allows for solvent-free and shorter reaction times with high yields.[25] Mechanosynthesis of metal oxide nanoparticles in the presence of Lewis bases has been extensively explored using planetary mills.[25] For example, Seyedi *et al.* demonstrated the synthesis of Fe_2O_3 nanoparticles by monitoring reaction time to produce smaller-size nanoparticles (12 nm, 4 nm) with moderate milling times of 2 and 5 h, respectively, using a planetary mill.[26] Recently, Bedoya *et al.*[7] reported the use of different reaction jars, steel and zirconia, to synthesise a mixture of magnetite/maghemite and hematite nanoparticles with nanoparticle size in a range of 6 to 12 nm after 12 hours of milling, respectively.[7] In Scheme 1, the introduction of a ball mill reduces the reaction time of a liquid-state (co-precipitation) synthesis of Fe_2O_3 nanoparticles into a fast single step that has a low energy consumption and is highly scalable and simple.[27] Baláž *et al.* utilised natural products (lichens, eggshell membranes, and

[a]*Research Centre for Synthesis and Catalysis, Department of Chemical Sciences, University of Johannesburg, Auckland Park, Johannesburg, 2006, South Africa. E-mail: bvatsha@uj.ac.za; Tel: +27 11 559 7656*

[b]*Microbiology and Environmental Biotechnology Group, Agricultural Research Council-Natural Resources and Engineering, Arcadia, Pretoria, 0083, South Africa*

[c]*Institute for Catalysis and Energy Solutions, College of Science, Engineering and Technology, University of South Africa, Florida, 1710, South Africa. E-mail: ndabab@unisa.ac.za; Tel: +27 11 043 2516*

[d]*Department of Environmental Sciences, College of Agriculture and Environmental Sciences, University of South Africa, Florida, 1710, South Africa*

† Electronic supplementary information (ESI) available. See DOI: https://doi.org/10.1039/d5ra02321a

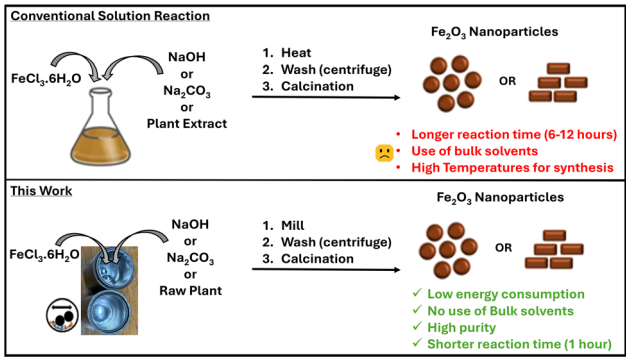

Scheme 1 Synthetic protocols of preparing Fe_2O_3 nanoparticles using liquid-state and solid-state reactions.

flowers) to synthesise silver nanoparticles.[28–31] This study employs *Artemisia afra* (*A. afra*), a medicinal plant, to develop metal oxide (Fe_2O_3) nanoparticles. Green synthetic methods are promising to provide control over nanoparticles formed without using auxiliaries, large amounts of solvents and trivial purification steps.[32] This, therefore, prompted us to investigate the mechanochemical synthesis of Fe_2O_3 nanoparticles by evaluating the parameters that influence the formation of nanoparticles: milling time, liquid-assisted grinding (LAG) and metal salt precursor. Lewis base compounds, sodium carbonate (Na_2CO_3), sodium hydroxide (NaOH) and phytochemicals from the medicinal plant, *Artemisia afra* were used for the reactions as structure director.[33]

2 Experimental

2.1 Materials and methods

Ferric chloride hexahydrate ($FeCl_3 \cdot 6H_2O$, Labchem), ferric nitrate nonahydrate ($Fe(NO_3)_3 \cdot 9H_2O$, Sigma-Aldrich) and ferric sulphate hydrate ($Fe_2(SO_4)_3 \cdot H_2O$, Sigma-Aldrich) were used as iron precursors and sodium hydroxide (NaOH, Rochelle Chemicals) or sodium carbonate (Na_2CO_3, Rochelle Chemicals) were used as base for the chemical synthesis of iron nanoparticles. Deionised water, acetonitrile (Sigma-Aldrich) and hexane (Sigma-Aldrich) were used for the liquid-assisted grinding (LAG). All chemicals used in this experiment were of analytical grade. Ariel parts of *A. afra* were collected from Eastern Cape in South Africa. To remove the soil debris, the plant material was rinsed with tap water followed by washing with distilled water three times. The rinsed plant material was then air-dried for a week and blended to powder and kept in the refrigerator until use. The reactants were milled using an IST636 mixer miller with steel milling jars and balls.

2.2 Synthesis of nanoparticles

1.4 mmol Ferric chloride hexahydrate ($FeCl_3 \cdot 6H_2O$) was used as an iron precursor and 4.4 mmol sodium hydroxide (NaOH) or 2.2 mmol sodium carbonate (Na_2CO_3) were used as base for the synthesis of iron nanoparticles as shown in eqn (I) and (II).[26,34]

$$2FeCl_3 \cdot 6H_2O + 6NaOH \rightarrow 2Fe(OH)_3 + 6NaCl + 12H_2O$$
$$2Fe(OH)_3 \rightarrow Fe_2O_3 + 3H_2O \quad (I)$$

$$2FeCl_3 \cdot 6H_2O + 3Na_2CO_3 \rightarrow Fe_2(CO_3)_3 + 6NaCl + 12H_2O$$
$$Fe_2(CO_3)_3 \rightarrow Fe_2O_3 + 3CO_2 \quad (II)$$

The model reactions were optimized by varying reaction time, size of the milling balls, addition of solvents (in the form of droplets). The model reaction was also adapted for the plant-mediated synthesis of iron oxide nanoparticles by altering the iron salt: plant material ratio for reaction in eqn (III).

$$FeCl_3 \cdot 6H_2O + \textit{Artemisia afra} \rightarrow Fe_2O_3 + \text{by-products} \quad (III)$$

The final as-milled product was washed with distilled water three times *via* centrifugation (4500 rpm for 10 minutes) and calcined at 500 °C for 4 hours. The calcined product was grinded to fine powder and characterized.

2.3 Characterization techniques

The diffraction pattern of grounded Fe_2O_3 nanoparticle samples were analysed by PANalytical Empyrean powder diffractometer fitted with Pixel detector, with Cu Kα ($\lambda = 0.154060$ nm) radiation source and operating at 40 kV and 40 mA conditions. The measurements were carried under Gonio scan axis with continuous scan, and 2θ range of 4 to 90°. The shape, particle size and distribution were investigated using transmission electron microscopy (TEM) using JEOL JEM-2100F transmission electron microscope operated at an acceleration voltage of 200 kV. The instrument had a charged coupled device (CCD) digital camera and an LaB6 source. The samples were dispersed in ethanol and placed onto a 200-mesh size copper grid coated with a thin layer of lacy carbon. The Fourier Transform Infrared (FTIR) spectra of samples were recorded on a Nicolet FTIR spectrometer (IS 50) at room temperature in the wavenumber range of 400–4000 cm^{-1} with a resolution of 4 cm^{-1}. The Raman spectrometer used is the Alpha300R Confocal Raman spectrometer, with 600 grooves per mm and a laser wavelength of 532 nm. A 50X objective was used and a 100-μm optical fiber which also acted as the entrance slit to the spectrometer.

3 Results and discussion

In our investigation, we have devised a synthetic method using a vibrational ball mill to synthesise iron(III) oxide nanoparticles in the presence of modulators such as Lewis bases and/or raw plant material (Fig. 1a). The base and metal precursor were milled at 23 Hz for an hour using 10 mm milling balls (×2) (Table S1†). The resulting product was washed and calcined at 500 °C to form Fe_2O_3 nanoparticles. Hydrous iron metal salt ($FeCl_3 \cdot 6H_2O$) is often called soft mechanochemistry.[25] Hydrate materials are beneficial for the mechanochemical induction of chemical reactions as they are said to be softer than their anhydrous form, thus assisting in having an active reactant surface for the reaction to occur. The use of alkali-metal hydroxide counter reactants such as NaOH can lead to the

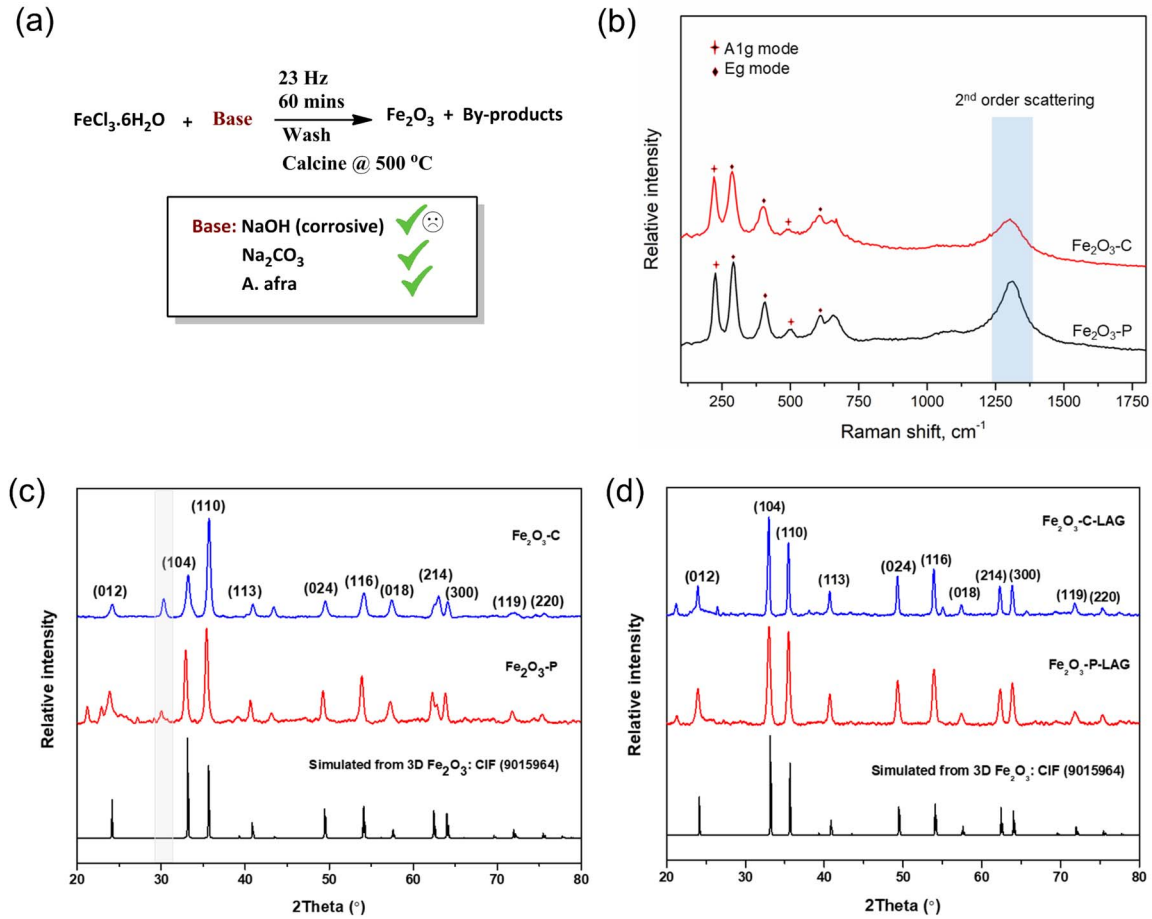

Fig. 1 (a) Chemical reactions of Fe_2O_3 nanoparticles using NaOH, Na_2CO_3 and plant material (*A. afra*) as a base. (b) Raman spectra of Fe_2O_3–C/P nanoparticles. (c) XRD pattern of neat Fe_2O_3–C/P, and (d) XRD pattern of LAG Fe_2O_3–C/P nanoparticles. LAG = Liquid Assisted Grinding.

caking of the milled powder and repress the reaction kinetics, impeded by the completion of the reaction during milling.[25] Alkali-metal carbonates such as Na_2CO_3 can also be used, forming soluble NaCl as a by-product. Na_2CO_3 is more advantageous than NaOH because it is less hygroscopic and corrosive than NaOH, and thus, easier to handle.[25] Thus, Na_2CO_3 was a more favourable base to use. *Artemisia afra* has previously been used in the synthesis of metal nanoparticles and its extracts have been found to have great antioxidant properties.[35–37] Thus, the plant material was evaluated to replace the chemical base (Na_2CO_3) and optimized by varying the iron salt:plant material ratio (Table S2†).

We used the powder X-ray diffraction (PXRD) analysis to understand the formation of iron nanoparticles. The diffraction patterns in Fig. 1c and d represent synthesised iron nanoparticles labelled Fe_2O_3–C and Fe_2O_3–P formed from using Na_2CO_3 and plant material (*A. afra*) as base, respectively. These PXRD patterns confirm the formation of the hematite (α-Fe_2O_3) nanoparticles and match very well with the simulated PXRD pattern from the crystal structure (CIF# 9015964) as well as reported hematite (α-Fe_2O_3) [ICSD:01-076-4579].[38] It was fascinating that using plant-containing compounds gave the same α-Fe_2O_3 nanoparticles as the chemical base, thus suggesting that the phytochemicals present in the *A. afra* are involved in the synthesis of nanoparticles. The optimum metal precursor:plant material ratio was 1 : 1 and the XRD patterns also confirms formation of hematite (Fig. S1.1 and S1.2†). The introduction of mechanochemistry has resulted in a shorter reaction time at ambient conditions in comparison to the longer reaction times used in planetary mills and solution-based reactions (8–24 h) reported in literature.[7,10,39,40] The plant-mediated synthesis of iron oxide nanoparticles as a reagent in the mechanochemical process offers a low-energy alternative, as it occurs near room temperature during milling. In contrast, plant extract-based green synthesis methods occur at elevated temperatures such as 80–85 °C, as reported by Patino-Ruiz *et al.* and Ndaba *et al.* to facilitate nanoparticle formation.[41,42] Interestingly, the nanoparticles prepared using neat grinding and liquid-assisted grinding (LAG) proved that these methods could be an alternative to solution/solvent-based synthesis.[43] Do and Friscic reported the limitations of LAG by explaining the reactant reactivity and solubility. To avoid slurry reactions, a small amount of liquid (0–1 $\mu L\ mg^{-1}$) should be used to facilitate transformations that are not possible through neat grinding and speed up reactions.[43] In this study, a liquid to solid ratio (η) of 0.10 $\mu L\ mg^{-1}$ was used for the chemical-mediated synthesis

and 0.13 μL mg^{-1} for the plant-mediated synthesis. The choice of solvent (water/acetonitrile/hexane) used in our reactions in Table S1† resulted in no obvious difference in PXRD patterns. Furthermore, acetonitrile resulted in a higher as-milled iron oxide yield (88%). We also observed the disappearance of a peak at $2\theta = 30°$ in the PXRD patterns in Fig. 1d when an additional liquid (20–50 μL) was used in the LAG reaction mixture. This explains the difference in the resulted purity of iron oxide nanoparticles. The diffraction patterns for neat grinding and LAG samples matched very well with slight changes by having a parent peak at $2\theta = 30°$ from traces of magnetite (neat grinding) and other overlapping peaks. The results suggested that LAG produces purer α-Fe_2O_3 phase than neat grinding, but it is difficult to account for the differences in morphological structure. To ascertain the role of mechanochemistry on the formation of the α-Fe_2O_3 phase, the reactants were kept in the reaction jars for 60 minutes (ageing) and then directly calcined at 500 °C using the same conditions as the milled α-Fe_2O_3 phase. In Fig. S1.3,† the collected XRD patterns labelled as A1 and A2, show the presence of Fe_2O_3 and by-products of sodium chloride (NaCl) salts. A possible reason for forming Fe_2O_3 is the open-air furnace calcination step, where the abundance of oxygen could react with metallic iron to form iron oxide nanoparticles. When the aged product (60 minutes) was washed (before calcination), almost all of it dissolved in water, which suggests little to no reaction between the starting material, thus negligible formation of the expected intermediate ($Fe(OH)_3$) due to no external energy input. In the case of the milled product, the intermediate $Fe(OH)_3$ was washed to remove the by-product NaCl (c) and further calcination step resulted in Fe_2O_3 nanoparticles. The PXRD results seen in Fig. S1.4† presents the use NaOH (c) and *A. afra* (d) during milling. The amorphous nature of the plant material (d) hinders the ability to detect the iron precursor post milling, and after calcination, the presence of Fe_2O_3 nanoparticles can be seen. This shows that milling is responsible for the formation of the intermediate ($Fe(OH)_3$) and calcination to produce Fe_2O_3 nanoparticles.

The phase identification of the synthesised Fe_2O_3 nanoparticles was further confirmed using Raman Spectroscopy. In Fig. 1b, the Raman spectra of α-Fe_2O_3 nanoparticles for both chemical base (Fe_2O_3–C) and plant-containing compounds (Fe_2O_3–P) exhibit similar characteristic peaks. The Raman signatures observed were A_{1g} and E_g modes corresponding to α-Fe_2O_3 nanoparticles. The peaks at 222 and 493 cm^{-1} were assigned to the A_{1g} mode, and peaks at 285, 397, 600 cm^{-1} were attributed to the E_g mode (Fe_2O_3–C).[44,45] When plant-containing compounds were used instead of a chemical base, the peaks shifted slightly. Peaks located at 226 and 500 cm^{-1} were assigned to the A_{1g} mode, and peaks at 291, 407, 616 cm^{-1} were assigned to the E_g mode (Fe_2O_3–P).[44,45] These Raman spectra are distinct signature peaks for the hematite polymorph structure.[44,45] We also note that the extraneous broad peaks between 600 cm^{-1} and 660 cm^{-1} could be overlapping peaks of magnetite with small traces present as observed from the PXRD. The broad and intense peak at 1303 cm^{-1} (Fe_2O_3–C) and 1309 cm^{-1} (Fe_2O_3–P) represents the second order scattering process emanated from α-Fe_2O_3.[44,45]

The morphological structures of the iron oxide nanoparticles prepared by neat grinding and LAG were captured using transmission electron microscopy (TEM). TEM measurements in Fig. 2a showed nanorods with average width = 20 nm and length diameter = 54 nm for neat grinding (solvent-free) when Na_2CO_3 base was used (a), but when *A. afra* was used, only extremely small nanoparticles were obtained (c). The addition of a small droplet of water in the LAG reaction formed oblong and spherical-like nanoparticles, which could be the result of agglomeration (b). The TEM images were processed through ImageJ software, where the estimated nanoparticle size distribution was between 10 and 70 nm with the average diameter of 30 nm for (g) Fe_2O_3–C (h), Fe_2O_3–C-LAG and (I) Fe_2O_3–P-LAG. Only sporadic examples of α-Fe_2O_3 nanorods have been reported through hydrothermal synthesis using NaOH, ammonium dihydrogen phosphate or tetrapropylammonium hydroxide as structure directing agents.[46–48] Another interesting recent work by Caspani *et al.* revealed the conversion approach of Fe^{3+} to Fe^{2+} in a hydrogen-based direct reduction method while preserving the shape and size of the nanoparticles for better applicability in biomedicine.[47] We further explored the role of different metal precursors: iron chloride, iron sulphate and iron nitrate for the formation of nanoparticles. The TEM images shown in Fig. S1.8† presents the chemical and plant-mediated mechanosynthesis using iron sulphate and iron nitrate. The morphological results suggest the change to hexagonal nanoparticles when iron sulphate precursor was used. On the other hand, the iron nitrate produced more spherically shaped nanoparticles for chemical-mediated mechanosynthesis. These observations are in line with a study by Lui *et al.* that investigated the effect of anions as structure directing agents to form α-Fe_2O_3 of different shapes.[49] The plant-mediated mechanosynthesis resulted in agglomerated spherical nanoparticles for both metal precursors. The TEM lattice fringe patterns captured were used to compute the interlayer spacing by employing Fast-Fourier Transform (FFT) method (Fig. S1.5†).[50] The calculations from measured TEM images gave interlayer fringe spacing values of 0.194 nm for Fe_2O_3–C (a); 0.116 nm for Fe_2O_3–C-LAG (b); and 0.229, 0.211 and 0.148 nm for Fe_2O_3–P-LAG (c) (Fig. S1.7†) which are comparable to the standard reference [ICSD:01-076-4579] and other similar work.[51] We speculate that the choice of using the chemical base and/or phytochemicals dictates the nanoparticle morphology formed. Depending on the structure director used, these further influence fast and/or slow nucleation and growth of nanoparticles. The reason for ultra-small nanoparticle formation is the presence of phytochemicals from the plant. *A. afra* corresponding to bioactive compounds such as flavonoids, terpenoids, phenolics and alkaloids, which play a role in the nucleation and stabilization of the nanoparticles.[42,51,52] When *A. afra* was used instead of a chemical base during nanoparticle formation, TEM images revealed no significant difference when comparing the morphology of the nanoparticles prepared by different types of solvents used for LAG reactions: water (Fig. 2b) and acetonitrile (Fig. S1.6b†). Only slight changes in the degree of agglomeration were observed during LAG reactions in the presence of water (Fig. 2c) and hexane (Fig. S1.6c†). The selected

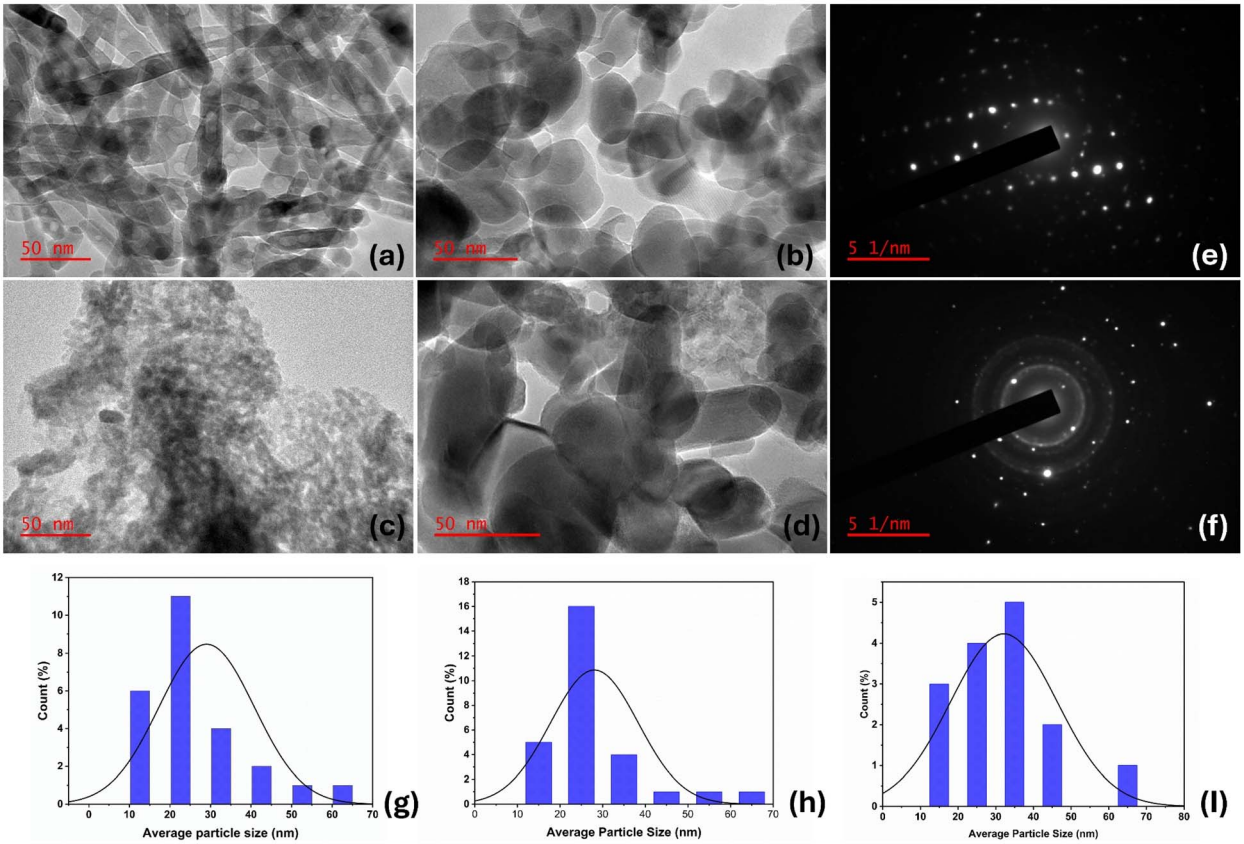

Fig. 2 TEM images of Fe_2O_3–C (a), Fe_2O_3–C-LAG (b), Fe_2O_3–P (c) and Fe_2O_3–P-LAG (d); SAED images of Fe_2O_3–C (e) and Fe_2O_3–P (f); distribution curve for Fe_2O_3–C (g), Fe_2O_3–C-LAG (h) and Fe_2O_3–P-LAG (I). Fe_2O_3–C = synthesised iron nanoparticles using chemical base (Na_2CO_3); Fe_2O_3–P = synthesised iron nanoparticles using plant material in a 1 : 1 metal precursor : *A. afra* ratio; LAG = liquid assisted grinding.

area electron diffraction (SAED) diffraction spots in Fig. 2 indicate a single-crystalline (e) and the appearance of polycrystalline rings (f) of the synthesised iron oxide nanoparticles and suggests high crystallinity of the prepared nanoparticles.

To decipher the elemental composition, chemical and electronic state of the constituent present in mechanosynthesised iron oxide nanoparticles, X-ray photoelectron spectroscopy (XPS) was used. The XPS survey scan for the sample Fe_2O_3–C produced by neat grinding as depicted in Fig. 3, shows the prominent peaks for iron oxides: C 1s, O 1s, and Fe 2p (a). The spin–orbit peaks of the Fe $2p_{(3/2)}$ and Fe $2p_{(1/2)}$ binding energies appeared at around 711.0 and 723.5 eV, respectively, corresponding to hematite (Fe^{3+}) electronic structure as seen in (b). The negligible subpeaks of the spin–orbit peaks of the Fe $2p_{(3/2)}$ and Fe $2p_{(1/2)}$ binding energies appeared at around 708 eV and 715 eV could result from traces of magnetite (Fe^{2+}). The spectrum in (c), shows the main peak at 285 eV assigned to carbon (C 1s) as reference for the charge correction. The spectrum in (d), shows detail peak for O 1s with subpeaks at 529.0 eV and 530.2 eV which was assigned to (O^{2-}) lattice oxygen and metal–oxygen species, respectively, and may indicate their presence in iron oxides. These observations agree well with both XRD and Raman as well as recent literature.[53]

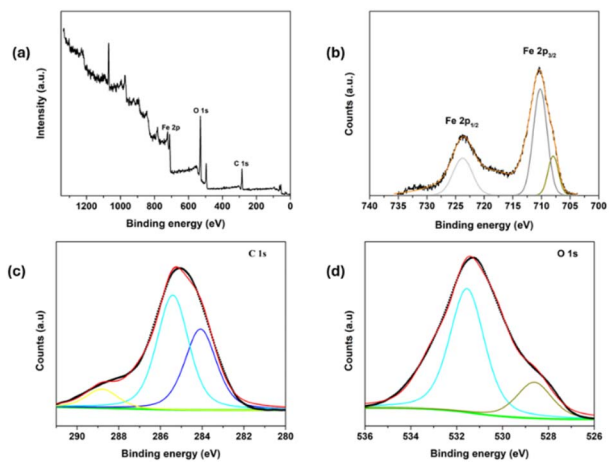

Fig. 3 XPS spectra of (a) XPS survey scan, (b) Fe 2p level, (c) C 1 s level, and (d) O 1 s level, of Fe_2O_3–C nanoparticles.

To determine the functionalities of the iron oxide nanoparticles synthesised, Fourier-transform infrared spectroscopy (FTIR) was utilised (Fig. S2†). For all the samples in Fig. S2,† the FTIR spectra depicts two distinct vibration bands located at 520 and 430 cm^{-1} which are attributed to metal–oxygen (Fe–O) bond from α-Fe_2O_3. There were additional bands at 1050 cm^{-1} and 1520 cm^{-1} attributed to the vibration in the OH groups from water and/or plant-containing compounds.[54,55] It is worth

noting that these additional peaks were only observed when the plant-containing compounds was used as base (Fe_2O_3–P), for both neat grinding and LAG.

4 Conclusions

We have successfully demonstrated the mechanosynthesis of iron oxide nanoparticles with chemical base and plant material containing phytochemicals using neat grinding and LAG reaction. We unveiled the effect of the chemical base and phytochemicals in forming iron oxide nanoparticles, leading to a change in the morphological shapes observed. Interestingly, nanorods were formed from neat grinding and changed to spherical-shaped nanoparticles in the LAG reaction medium when a chemical base was used. We investigated, for the first time, plant-mediated synthesis of α-Fe_2O_3 nanoparticles using *A afra* as a powder in a mechanochemical reaction. This approach suggested the capabilities of controlling the shape/size of the formed nanoparticles by using different metal precursors during iron oxide nanoparticle formation. This is particularly important as the shape and size of nanoparticles influence their magnetic properties, which is important for the biomedical industry. The most dominant polymorph formed in both chemical and plant-based synthesis was hematite (α-Fe_2O_3) nanoparticles. These results have unveiled a new synthetic approach for preparing iron oxide nanoparticles of various shapes using mechanochemistry. Further studies should be focused on an in-depth understanding of the role played by the chemical and plant as a base in nucleation and nanoparticle growth during mechanochemistry as well as other contributing parameters related to milling process.

Data availability

The data supporting this article has been included as part of the ESI.†

Author contributions

BN and BV conceptualised the project. TMR conducted the experiments and drafted the manuscript. AR, BN, BV and TMR edited the final draft. All authors have approved the final version of the manuscript.

Conflicts of interest

There is no conflict of interest to declare.

Acknowledgements

Authors would like to acknowledge the NRF-Thuthuka funding for this project, under Grant No. 138433 and 129651, and the Research Centre for Catalysis. Authors also thank the University of Johannesburg and the Agricultural Research Council for access to their laboratories and funding.

References

1 I. Khan, S. Morishita, R. Higashinaka, T. D. Matsuda, Y. Aoki, E. Kuzmann, Z. Homonnay, S. Katalin, L. Pavić and S. Kubuki, *J. Magn. Magn. Mater.*, 2021, **538**, 168264–168275.
2 L. MacHala, J. Tuček and R. Zbořil, *Chem. Mater.*, 2011, **23**, 3255–3272.
3 H. M. Torres Galvis, J. H. Bitter, C. B. Khare, M. Ruitenbeek, A. I. Dugulan and K. P. de Jong, *Science*, 2012, **335**, 835–838.
4 S. Malik, K. Muhammad and Y. Waheed, *Molecules*, 2023, **28**, 661–686.
5 M. Xu, Q. Zhang, X. Lin, Y. Shang, X. Cui, L. Guo, Y. Huang, M. Wu and K. Song, *Plants*, 2023, **12**, 778–800.
6 S. Zanganeh, G. Hutter, R. Spitler, O. Lenkov, M. Mahmoudi, A. Shaw, J. S. Pajarinen, H. Nejadnik, S. Goodman, M. Moseley, L. M. Coussens and H. E. Daldrup-Link, *Nat. Nanotechnol.*, 2016, **11**, 986–994.
7 P. A. Calderón Bedoya, P. M. Botta, P. G. Bercoff and M. A. Fanovich, *J. Alloys Compd.*, 2023, **939**, 168720–168726.
8 D. Bokov, A. Turki Jalil, S. Chupradit, W. Suksatan, M. Javed Ansari, I. H. Shewael, G. H. Valiev and E. Kianfar, *Adv. Mater. Sci. Eng.*, 2021, **2021**, 1–21.
9 P. Badanayak and J. V Vastrad, *Pharm. Innov.*, 2021, **10**, 1023–1027.
10 B. H. Hui and M. N. Salimi, *IOP Conf. Ser.:Mater. Sci. Eng.*, 2020, **743**, 012036–012049.
11 S. Qasim, A. Zafar, M. S. Saif, Z. Ali, M. Nazar, M. Waqas, A. U. Haq, T. Tariq, S. G. Hassan, F. Iqbal, X. G. Shu and M. Hasan, *J. Photochem. Photobiol., B*, 2020, **204**, 111784–111794.
12 F. Ozel, H. Kockar and O. Karaagac, *J. Supercond. Novel Magn.*, 2015, **28**, 823–829.
13 E. Aivazoglou, E. Metaxa and E. Hristoforou, *AIP Adv.*, 2017, **8**, 048201–048214.
14 C. Diaz, M. L. Valenzuela and M. Laguna-Bercero, *Int. J. Mol. Sci.*, 2022, **23**, 1–29.
15 A. Moores, *Curr. Opin. Green Sustainable Chem.*, 2018, **12**, 33–37.
16 P. F. M. De Oliveira, R. M. Torresi, F. Emmerling and P. H. C. Camargo, *J. Mater. Chem. A*, 2020, **8**, 16114–16141.
17 Q. Cao, J. L. Howard, D. E. Crawford, S. L. James and D. L. Browne, *Green Chem.*, 2018, **20**, 4443–4447.
18 S. J. Lyle, T. M. Osborn Popp, P. J. Waller, X. Pei, J. A. Reimer and O. M. Yaghi, *J. Am. Chem. Soc.*, 2019, **141**, 11253–11258.
19 A. M. Asiri, W. A. Adeosun, S. B. Khan, K. A. Alamry, H. M. Marwani, S. M. Zakeeruddin and M. Grätzel, *Sci. Rep.*, 2022, **12**, 1–10.
20 T. Seo, T. Ishiyama, K. Kubota and H. Ito, *Chem. Sci.*, 2019, **10**, 8202–8210.
21 P. Shafiee, S. M. Alavi and M. Rezaei, *Int. J. Hydrogen Energy*, 2021, **46**, 3933–3944.
22 J. Kim, J. Ha, J. H. Lee and H. R. Moon, *Nano Res.*, 2021, **14**, 411–416.
23 S. Chaemchuen, K. Zhou, M. S. Yusubov, P. S. Postnikov, N. Klomkliang and F. Verpoort, *Microporous Mesoporous Mater.*, 2019, **278**, 99–104.

24 J. L. Do and T. Friščić, *ACS Cent. Sci.*, 2017, **3**, 13–19.
25 T. Tsuzuki, *Commun. Chem.*, 2021, **4**, 143–153.
26 M. Seyedi, S. Haratian and J. V. Khaki, *Procedia Mater. Sci.*, 2015, **11**, 309–313.
27 M. A. A. Mohamed, H. A. A. Saadallah, I. G. Gonzalez-Martinez, M. Hantusch, M. Valldor, B. Büchner, S. Hampel and N. Gräßler, *Green Chem.*, 2023, **25**, 3878–3887.
28 M. Goga, M. Baláž, N. Daneu, J. Elečko, Ľ. Tkáčiková, M. Marcinčinová and M. Bačkor, *Mater. Sci. Eng., C*, 2021, **119**, 111640–111648.
29 M. Baláž, M. Goga, M. Hegedüs, N. Daneu, M. Kováčová, L. Tkáčiková, L. Balážová and M. Bačkor, *ACS Sustain. Chem. Eng.*, 2020, **8**, 13945–13955.
30 M. Baláž, N. Daneu, Ľ. Balážová, E. Dutková, Ľ. Tkáčiková, J. Briančin, M. Vargová, M. Balážová, A. Zorkovská and P. Baláž, *Adv. Powder Technol.*, 2017, **28**, 3307–3312.
31 M. Baláž, Z. Bedlovičová, N. Daneu, P. Siksa, L. Sokoli, Ľ. Tkáčiková, A. Salayová, R. Džunda, M. Kováčová, R. Bureš and Z. Bujňáková, *Nanomaterials*, 2021, **11**, 1139–1163.
32 A. Kumar, S. Dutta, S. Kim, T. Kwon, S. S. Patil, N. Kumari, S. Jeevanandham and I. S. Lee, *Chem. Rev.*, 2022, **122**, 12748–12863.
33 G. V. Patil, S. K. Dass and R. Chandra, *J. Pharmacogenomics Pharmacoproteomics*, 2011, **2**, 1–22.
34 P. A. Calderón Bedoya, P. M. Botta, P. G. Bercoff and M. A. Fanovich, *J. Alloys Compd.*, 2021, **860**, 157892–157902.
35 E. E. Elemike, D. C. Onwudiwe, A. C. Ekennia and A. Jordaan, *IET Nanobiotechnol.*, 2018, **12**, 722–726.
36 M. C. Martini, T. Zhang, J. T. Williams, R. B. Abramovitch, P. J. Weathers and S. S. Shell, *J. Ethnopharmacol.*, 2020, **262**, 113191–113196.
37 N. F. Kane, M. C. Kyama, J. K. Nganga, A. Hassanali, M. Diallo and F. T. Kimani, *S. Afr. J. Bot.*, 2019, **125**, 126–133.
38 K. Tharani and L. C. Nehru, *Int. J. Adv. Res. Phys. Sci.*, 2015, **2**, 47–50.
39 A. Zolriasatein, A. Shokuhfar, F. Safari and N. Abdi, *Micro Nano Lett.*, 2018, **13**, 448–451.
40 A. P. Lagrow, M. O. Besenhard, A. Hodzic, A. Sergides, L. K. Bogart, A. Gavriilidis and N. T. K. Thanh, *Nanoscale*, 2019, **11**, 6620–6628.
41 D. Patiño-Ruiz, L. Sánchez-Botero, L. Tejeda-Benitez, J. Hinestroza and A. Herrera, *Environ. Nanotechnol., Monit. Manage.*, 2020, **14**, 100377–100386.
42 B. Ndaba, A. Roopnarain, B. Vatsha, S. Marx and M. Maaza, *ACS Agric. Sci. Technol.*, 2022, **2**, 1218–1229.
43 J. L. Do and T. Friščić, *ACS Cent. Sci.*, 2017, **3**, 13–19.
44 Y. Cho and Y. Huh, *Bull. Korean Chem. Soc.*, 2009, **30**, 1413–1415.
45 P. Kumar, H. No-Lee and R. Kumar, *J. Mater. Sci.: Mater. Electron.*, 2014, **25**, 4553–4561.
46 C. D. Powell, A. W. Lounsbury, Z. S. Fishman, C. L. Coonrod, M. J. Gallagher, D. Villagran, J. B. Zimmerman, L. D. Pfefferle and M. S. Wong, *Nano Convergence*, 2021, **8**, 8–16.
47 S. Caspani, F. J. Fernández-Alonso, S. M. Gonçalves, C. Martín-Morales, B. Cortes-Llanos, B. J. C. Vieira, J. C. B. Waerenborgh, L. C. J. Pereira, A. Apolinario, J. P. Araújo, M. V. Gómez-Gaviro, V. Torres-Costa, M. J. Manso Silván and C. T. de Sousa, *ACS Appl. Mater. Interfaces*, 2025, **17**, 16602–16615.
48 Z. Zhong, J. Ho, J. Teo, S. Shen and A. Gedanken, *Chem. Mater.*, 2007, **19**, 4776–4782.
49 J. Liu, H. Yang and X. Xue, *CrystEngComm*, 2019, **21**, 1097–1101.
50 Q. Zhang, R. Bai, B. Peng, Z. Wang and Y. Liu, *Micron*, 2023, **166**, 103402–103413.
51 B. Shelembe, R. Moodley and H. Chenia, *S. Afr. J. Chem.*, 2023, **77**, 119–125.
52 N. Q. Liu, F. Van der Kooy and R. Verpoorte, *S. Afr. J. Bot.*, 2009, **75**, 185–195.
53 X. Yan, G. Li, K. Shen, C. Wang and K. Wang, *Green Chem.*, 2023, **25**, 9394–9404.
54 G. C. Fard, M. Mirjalili and F. Najafi, *Bulg. Chem. Commun.*, 2018, **50**, 251–261.
55 A. Lassoued, B. Dkhil, A. Gadri and S. Ammar, *Results Phys.*, 2017, **7**, 3007–3015.